ARTICLE

Piezoelectric Energy Harvesting Using Solar Radiation Pressure Enhanced by Surface Plasmons at Visible to Near-infrared Wavelengths†

Received 00th January 20xx,
Accepted 00th January 20xx

DOI: 10.1039/x0xx00000x

Jae-Hoon Ryu,[a,b] Ha Young Lee,[a,b] Sung-Hyun Kim,[a,b] Jeong-Yeon Lee,[a,b] Jun-Hyeon Jang,[a] Hyung Soo Ahn,[a] Sun-Lyeong Hwang,[c] Robert A. Taylor,*[d] Dong Han Ha*[e] and Sam Nyung Yi*[a,b]

A light-pressure electric generator (LPEG) device, which harvests piezoelectric energy using solar radiation enhanced by surface plasmons (SPs), is demonstrated. The design of the device was motivated by the need to drastically increase the power output of existing piezoelectric devices based on SP resonance. The LPEG device was fabricated by forming a crater structure capable of concentrating light on a GaAs (100) substrate and by sequentially depositing layers to form an indium tin oxide (ITO)/Ag/Pb (Zr,Ti)O_3 (PZT)/Pt/Ti structure. The solar radiation pressure can be used as an energy source by employing an ITO/Ag double layer to excite the SPs in the near-infrared (NIR) and visible light regions. The LPEG with the ITO layer generates an open-circuit voltage of 295 mV, a short-circuit current of 3.78 μA, and power of 532.3 μW/cm^2 under a solar simulator. The power of the LPEG device incorporating the ITO layer increased by 38% compared to the device without the ITO layer. The effect of the ITO layer on the electrical output of the LPEG was analysed in detail by measuring the electrical output when visible and NIR light were incident on the device using optical bandpass filters. In addition, finite-difference time-domain (FDTD) simulation confirmed that the pressure of the incident light can be further amplified by the ITO/Ag double layer. Finally, the energy harvested from the LPEG was stored in capacitors to successfully illuminate red light-emitting diodes (LEDs).

Introduction

In recent decades, remarkable improvements in medical technology and the quality of life have resulted in the rapid growth of the world population and, consequently, energy consumption.[1] On the other hand, fossil fuels are being gradually depleted, and environmental pollution and climate change problems are worsening owing to the use of energy sources based on fossil fuels. Therefore, the development of alternative renewable energy sources or energy harvesting technologies are essential for the future.[2,3] Renewable energy sources include solar radiation,[4,5] wind,[6] water flow,[7] heat,[8] and hydrogen,[9] of which solar radiation is the most accessible and eco-friendly energy source on Earth.[10,11] Typical technologies for harvesting solar energy include solar cells that convert light energy into electrical energy,[12] and solar thermal technology, which converts absorbed solar light into thermal energy.[13] More recently, solar radiation pressure (SRP) has been used as an energy source to propel solar sails in space.[14] Because the SRP reaching the earth's surface is very weak, approximately 4.6 μPa, the application thereof is limited. However, considering that the radiation pressure is proportional to $|E|^2$ (where E is the electric field), SRP could be expected to become a useful energy source provided it is significantly amplified.

The excitation of surface plasmons (SPs), a phenomenon in which free electrons collectively oscillate on a metal surface when light is incident on a dielectric-metal interface, has the effect of greatly amplifying the intensity of the electric field near the metal surface.[15] SPs are classified as a propagating surface plasmon transmitted in the form of a surface plasmon polariton along the dielectric-metal interface and the localised surface plasmon, oscillation of charges confined to a nanosized metal surface.[16] In particular, noble metal nanoparticles (NPs) such as Ag and Au generate SPs when the incident light consists of electromagnetic waves in the visible region.[17,18] In addition, the wavelength of the generated SPs varies depending on the size, shape, spacing, and the dielectric medium surrounding the metal NPs.[19,20] The strong amplification of the electric field around the metal NPs by SPs has found application in surface-enhanced Raman spectroscopy (SERS)[21] and enhancement of the solar cell efficiency.[22] For example, Lee *et al*. fabricated a SERS substrate based on gold nanostar assemblies on metal films and used it for the ultrasensitive detection of target

[a] *Major of Nano-Semiconductor Engineering, Korea Maritime & Ocean University (KMOU), Busan 49112, Republic of Korea*
E-mail: snyi@kmou.ac.kr
[b] *Interdisciplinary Major of Maritime AI Convergence, Korea Maritime & Ocean University (KMOU), Busan 49112, Republic of Korea*
[c] *Department of ICT Convergence Engineering, Kangnam University (KNU), Yongin 16979, Republic of Korea*
[d] *Department of Physics, University of Oxford, Parks Road, Oxford OX1 3PU, United Kingdom*
E-mail: robert.taylor@physics.ox.ac.uk
[e] *Division of Advanced Technology, Korea Research Institute of Standards and Science (KRISS), Daejeon 34113, Republic of Korea.*
E-mail: dhha@kriss.re.kr

† Electronic supplementary information (ESI) available. See DOI: http://doi.org/x0xx00000x

molecules.[23] Hao *et al*. achieved a current density of 23.34 mA/cm^2 and power conversion efficiency of 16.53% by integrating core–shell tetrahedral nanostructures into a perovskite solar cell.[24] However, because metals experience large optical losses and have high negative real-part permittivities, strong electric field amplification by SPs cannot be expected in the NIR region.[25]

Transparent conductive oxides (TCOs) such as Al:ZnO, Ga:ZnO, and indium tin oxide (ITO) exhibit excellent electrical conductivity and high light transmittance in the visible region, and their optical properties can be controlled by adjusting the extent of doping or their chemical composition.[26-28] Thus, many studies have been conducted on NIR plasmonic materials because TCOs exhibit low optical loss, particularly in the NIR region.[29] In most TCO materials, the crossover wavelength (the wavelength at which the real part of the permittivity switches from positive to negative for certain materials) exists in the NIR region.[30] Furthermore, the behaviour of a TCO approximates that of a metal when the wavelength of the incident light is longer than the crossover wavelength.[31] In addition, because TCOs have a positive permittivity for visible light, they are also used as dielectric materials.[32,33] Currently, the most popular TCO material is ITO because it can be heavily doped.[28,34] Ma *et al*. adjusted the surface plasmon resonance (SPR) frequency in the NIR region by controlling the dopant concentration, and the size and shape of ITO NPs.[35] Hong *et al*. studied the effect of the dielectric environment on the optical properties of the Ag layer by comparing the SPR frequency and absorption intensity of the ITO/Ag and TiO_2/Ag bilayers in the visible region.[36]

In previous studies, we amplified the laser radiation pressure sufficiently to stimulate $Pb(Zr,Ti)O_3$ (PZT) by forming Pt and Ni layers with nanoroughness on the slope of the crater structure.[37,38] Moreover, by optimising the type and thickness of the upper electrode such that the SPs are well developed in the visible band, a power density of 396 μW/cm^2 was obtained upon irradiation with the solar simulator.[39] However, because the output of SRP-based piezoelectric devices is still insufficient for real-life applications, improvements to increase the power output are required. To date, we have only used light from the visible wavelength range, but because the NIR region accounts for more than 50% of the total energy of sunlight reaching the earth's surface,[40,41] the power of an LPEG is expected to be greatly improved by using both visible and NIR light together. In this study, to improve the output of a light-pressure electric generator (LPEG), a rough ITO/Ag bilayer capable of generating SPs in the NIR and visible regions was created on the inner slope of the crater. By forming a rough ITO layer with high transmittance in the visible region on the rough Ag layer, the total pressure of the incident light was enhanced by generating SPs in the NIR and visible regions from the ITO and Ag layers, respectively. The electric field distribution in the Ag and ITO layers as a function of the wavelength of light was analysed by conducting finite-difference time-domain (FDTD) simulation, and the dependence of the device output on the wavelength was confirmed by separating the sunlight into its wavelength components using optical filters. In addition, the possibility of real-life application was demonstrated by illuminating red light-emitting diodes (LEDs) by harvesting electrical energy with the LPEG.

Experimental details

Fabrication of LPEG

Firstly, a crater structure was fabricated on a GaAs (100) substrate by wet chemical etching,[42] and then a Pt (100 nm)/Ti (10 nm) layer was deposited on this substrate using e-beam evaporation. Next, a sol-gel solution of PZT (Zr: Ti=52:48, 0.4 mol/L, Quintess) was spin-coated onto the Pt/Ti layer at 3000 rpm for 45 s, followed by pyrolysis processes on a hot plate at 250 °C for 5 min and 300 °C for 3 min. This was followed by rapid thermal annealing at 650 °C for 5 min under a nitrogen atmosphere. To fabricate a PZT layer with the appropriate thickness and excellent piezoelectric properties, the spin-coating and RTA processes were repeated four times. Subsequently, a Ag layer with a thickness of 60 nm was deposited by e-beam evaporation using a shadow mask. The final layer was deposited by spin coating ITO NPs in ethanol solution (Sn 10 %, particle size 20–70 nm, RNDKOREA) diluted to 10 wt% at 3000 rpm for 40 s, with subsequent exposure to heat on a hot plate at 130 °C for 5 min. The spin-coating and heat-treatment processes were repeated twice to obtain an ITO layer with the desired roughness and thickness. A detailed schematic of the experimental process is presented in Fig. S1 in the Supporting Information.

Simulations

We investigated the optical properties of the ITO layer and the electric field distribution according to the wavelength of the light source for 10,000 fs using the commercial Lumerical FDTD software. Perfectly matched layers with completely absorbed light were applied to the upper and lower layers of the FDTD region. The electric field monitor was set to include part of the object, and the total-field scattered field source propagated along the y-axis at the top of the object. The materials of the structure were applied using built-in tools (GaAs and Ag), and ITO was applied by importing the complex refractive index data library of the spectroscopic ellipsometry software (J.A. Woollam Co.). The model was constructed by referencing the FE-SEM images to obtain the size and shape of the Ag and ITO layers.

Characterisation

The overall crater structure was observed using a high-resolution 3D microscopy (VHX-7000, KEYENCE). The cross-sectional structure of the crater and the roughness of the Ag and ITO layers were measured using field-emission scanning electron microscopy (FE-SEM; CLARA, Tescan). The voltage and current output of the LPEG by solar radiation were measured using a source meter (2400, Keithley), and the crystallinity of the PZT layer was confirmed using a Raman spectrometer (UniDRON, Uninanotech). The variation of the output characteristics of the LPEG according to the solar radiation wavelength were measured using an optical filter (Edmond Optics).

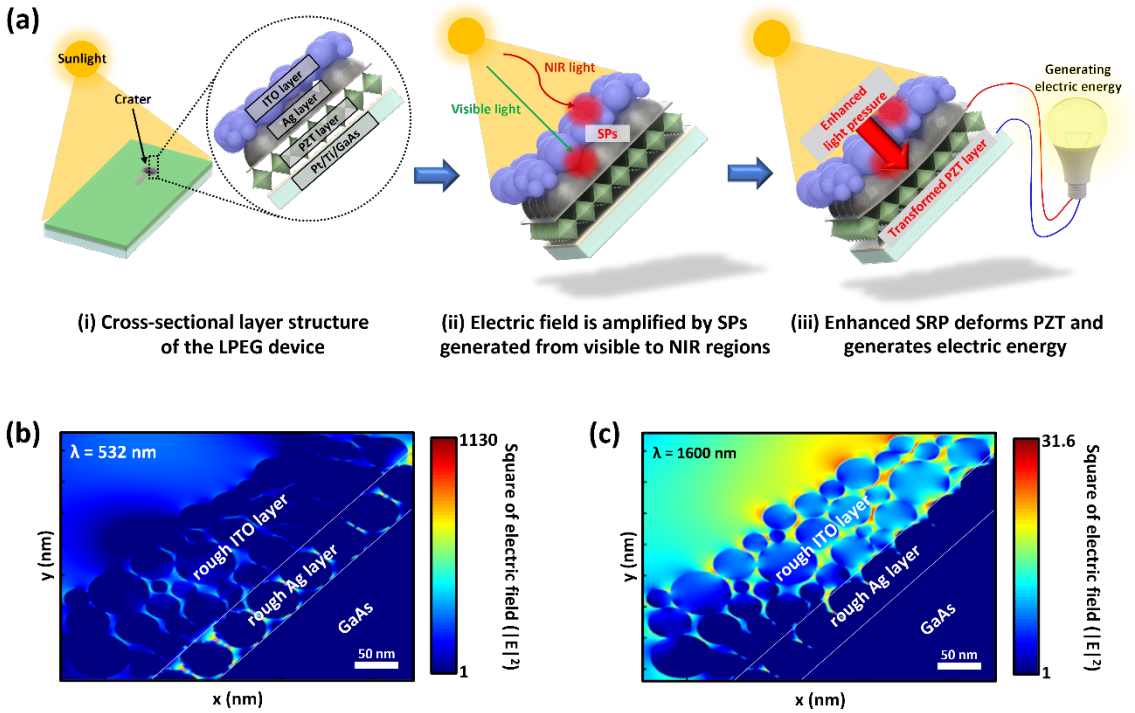

Fig. 1. (a) Schematic diagram of the working mechanism of the LPEG with the ITO/Ag double layer. FDTD simulation results (on a logarithmic scale) of the electric field distribution for wavelengths of (b) 532 and (c) 1600 nm.

Results and discussion

Fig. 1(a) shows schematic diagrams of the cross-sectional layer structure and the operating mechanism of the LPEG device that produces electrical energy via SRP. (i) The unique structure we created to amplify the weak SRP was designed as a crater-type LPEG device with ITO/Ag/PZT/Pt/Ti layers in the crater structure. The Ag and ITO layers that amplify the SRP are composed of grains less than 100 nm in size. (ii) The electric field could be amplified by exciting the SPs with visible light using a metal layer of Ag, Au, or Pt with a surface roughness of less than 100 nm.[37,38] We fabricated an energy-harvesting device with improved efficiency using a wide range of solar radiation by amplifying the SRP in both the visible and NIR regions using an ITO/Ag double layer. The device is designed such that when sunlight illuminates the inside of the crater, NIR light generates SPs in the ITO layer, whereas the visible light penetrates the ITO layer and generates SPs in the Ag layer. Therefore, the intensity of the electric field of the solar radiation is expected to be amplified from the visible to the NIR light region. (iii) Because the light pressure is proportional to $|E|^2$ ($P_{ressure} = E^2/c^2\mu_0$), the intensity of the electric field, that is, the SPs are amplified sufficiently to deform the piezoelectric material beneath the ITO/Ag layer, electrical energy is generated as a result of the piezoelectric effect in the PZT layer.

We performed FDTD simulations to analyse the response of the LPEG according to the wavelength of light, and the results are shown in Fig. 1(b) and (c) for 532 nm (visible) and 1600 nm (NIR) light sources, respectively. For the simulation, the ITO layer was composed as randomly placing ITO NPs with a diameter of 20–70 nm, and the Ag layer was reproduced by setting grains with a diameter of 60 nm by referring to the FE-SEM results. As shown in Fig. 1(b), the visible light penetrated the ITO layer, thereby significantly amplifying the electric field strength in the narrow gap between the Ag grains. On the other hand, as shown in Fig. 1(c), the NIR light amplified the electric field between the air/ITO interface and the ITO NPs, although this amplification was weaker than that in the Ag layer. In other words, Fig. 1(b) and (c) indicate that both visible and NIR light can be used as energy sources by incorporating a rough ITO/Ag double-layered structure.

Fig. 2(a) shows a high-resolution 3D optical image of the crater, which is the operating part of the device based on the mechanism described in Fig. 1(a). The crater structure has an open top and bottom and becomes narrower toward the bottom. The depth of the crater is approximately 95 μm, as shown in Fig. S2 in the Supporting Information, which almost coincides with the thickness of the GaAs substrate after the lapping process. Fig. 2(b) shows a cross-sectional FE-SEM image of the inside of the crater. The slope of the crater was composed of ITO/Ag/PZT/Pt/Ti/GaAs layers, and the thicknesses of the PZT and ITO layers were approximately 900 and 500 nm, respectively. Fig. 2(c) shows a top-view FE-SEM image of the ITO NPs deposited inside the crater and shows that ITO NPs with sizes of 20–70 nm overlap each other. Fig. 2(d) shows the Raman spectrum of the PZT layer measured using 532 nm laser light at room temperature. The Raman modes of E(2TO), ET+B1, A1(2TO), A1(2TO), and A1(3LO) of PZT are clearly observed at Raman shifts of 205, 275, 330, 591, and 740 cm^{-1}.[43,44] Our analysis of the Raman spectrum revealed that the PZT inside the crater exists in the tetragonal phase with excellent piezoelectric

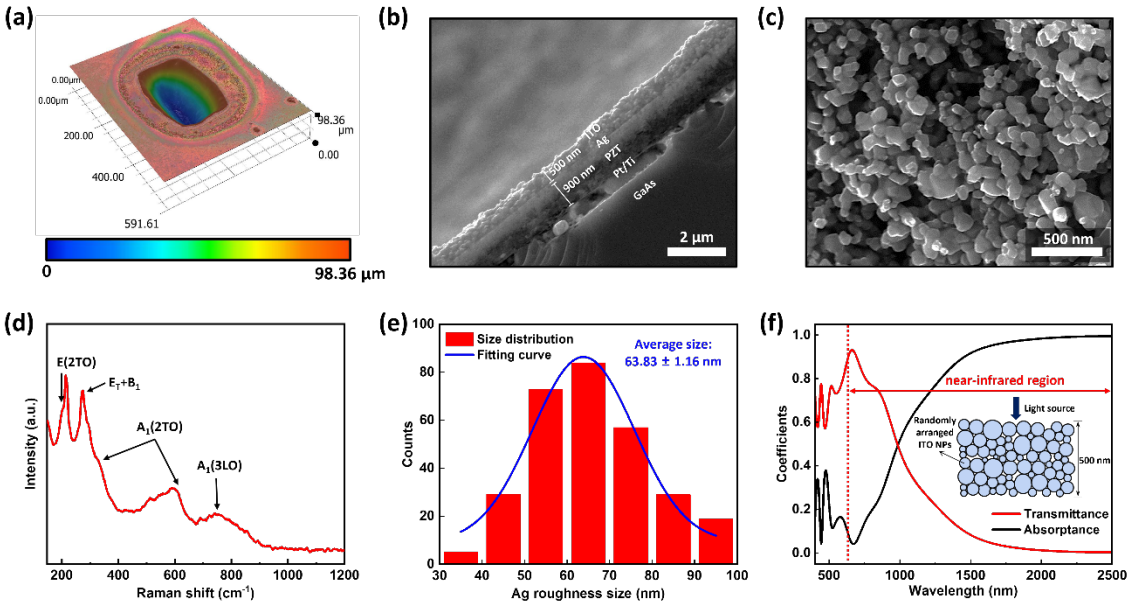

Fig. 2. (a) High-resolution 3D optical image of overall view of the device. (b) Cross-sectional FE-SEM image of the inside of a crater. (c) Top-view FE-SEM image of the ITO layer. (d) Raman spectrum of the PZT layer inside the crater. (e) Particle size distribution of the rough Ag layer and fitted curve of the as-deposited Ag layer. (f) Transmittance (red) and absorptance (black) of the rough ITO layer computed using the FDTD method.

properties.[45] As shown in the top-view FE-SEM image acquired after deposition of the Ag layer (Supporting Information, Fig. S3(a) and (b)), the outer surface of the crater is a relatively dense thin film with few grains, whereas the inner surface of the crater is composed of numerous nanoscale grains. The nanoscale roughness inside the crater was formed when the PZT sol-gel solution was spin-coated.[38] Fig. 2(e) shows the roughness size distribution of the Ag layer obtained from the FE-SEM image in Fig. S3(b). The surface of the Ag layer is mainly composed of numerous grains with sizes ranging from 40 to 90 nm, with an average size of 63.83 ± 1.16 nm. These large variations in the roughness can greatly enhance the electric field at the surface, as the SP is excited by the visible wavelength component of solar radiation.[46,47] An FDTD simulation was performed to determine the optical properties of the top ITO layer. ITO NPs with a size of 20–70 nm were randomly placed to form a layer with a thickness of 500 nm, and the absorptance was calculated using the equation Absorptance = 1 − (Transmittance + Reflectance). Reflection hardly occurred at any wavelength (Supporting information, Fig. S4). Fig. 2(f) shows the transmittance (red curve) and absorptance (black curve) of the 500 nm thick ITO layer. As shown in the figure, because the ITO layer mostly transmitted light with wavelengths in the range of 400 to 600 nm, the intensity of the visible light incident on the surface of the Ag layer was hardly reduced. However, the absorptance at the ITO layer gradually increased as the wavelength of the incident light became longer, and most of the light was absorbed when the wavelength of the incident light was approximately 1500 nm or longer. This indicates that the NIR component of the incident light is absorbed by the ITO layer to excite the SPs.[35] In other words, the Ag layer amplifies the visible light component of the incident light, whereas the ITO layer amplifies the NIR component of the incident light at a lower amplification rate than the visible component. These results confirm that an LPEG with a double-layered structure comprising a rough ITO layer on a Ag layer can contribute to increasing the efficiency by using incident light with both visible and NIR wavelengths.

Fig. 3(a) shows a schematic diagram of the experimental setup for measuring the device output to confirm the effect of the ITO layer. The wavelengths from the solar simulator (AM 1.5G) were classified into four groups using various types of optical bandpass filters: band I (300–2500 nm: solar light), band II (400–750 nm: visible light), band III (750–2500 nm: entire NIR region), and band IV (1000–2500 nm: part of the NIR region). Fig. 3(b) and (c) show the open-circuit voltage (V_{oc}) and short-circuit current (I_{sc}) of the LPEG according to the wavelength band of the incident light with and without the ITO layer, respectively. All electrical outputs of the LPEG were measured before and after the formation of the ITO layer on the same device and were self-rectified.[39] For band I, the LPEG with the ITO layer generated V_{oc} of 295 mV and I_{sc} of 3.78 μA, whereas the LPEG without the ITO layer generated only V_{oc} of 253 mV and I_{sc} of 3.25 μA. Hence, both V_{oc} and I_{sc} of the LPEG with the ITO layer increased by approximately 16% compared with the LPEG without the ITO layer. For band II, the LPEG with the ITO layer generated V_{oc} of 264 mV and I_{sc} of 2.6 μA, whereas the LPEG without the ITO layer generated a lower V_{oc} of 236 mV and I_{sc} of 2.52 μA. The presence of the ITO layer slightly increases both the voltage and current; that is, the intensity of the electric field is enhanced by the SPs generated at the ITO/Ag interface. This is attributed that ITO has high transmittance and positive real part of the permittivity in the visible region (functioning as a dielectric layer).[32,33,36] An FDTD simulation was performed to confirm the electric-field distribution inside the crater with and without the ITO layer in the visible band. The electric field distributions in the Ag layer at 532 nm, and in the Ag layer, and ITO/Ag layer at 633 nm are shown in Fig. 3(d)–(f). For incident

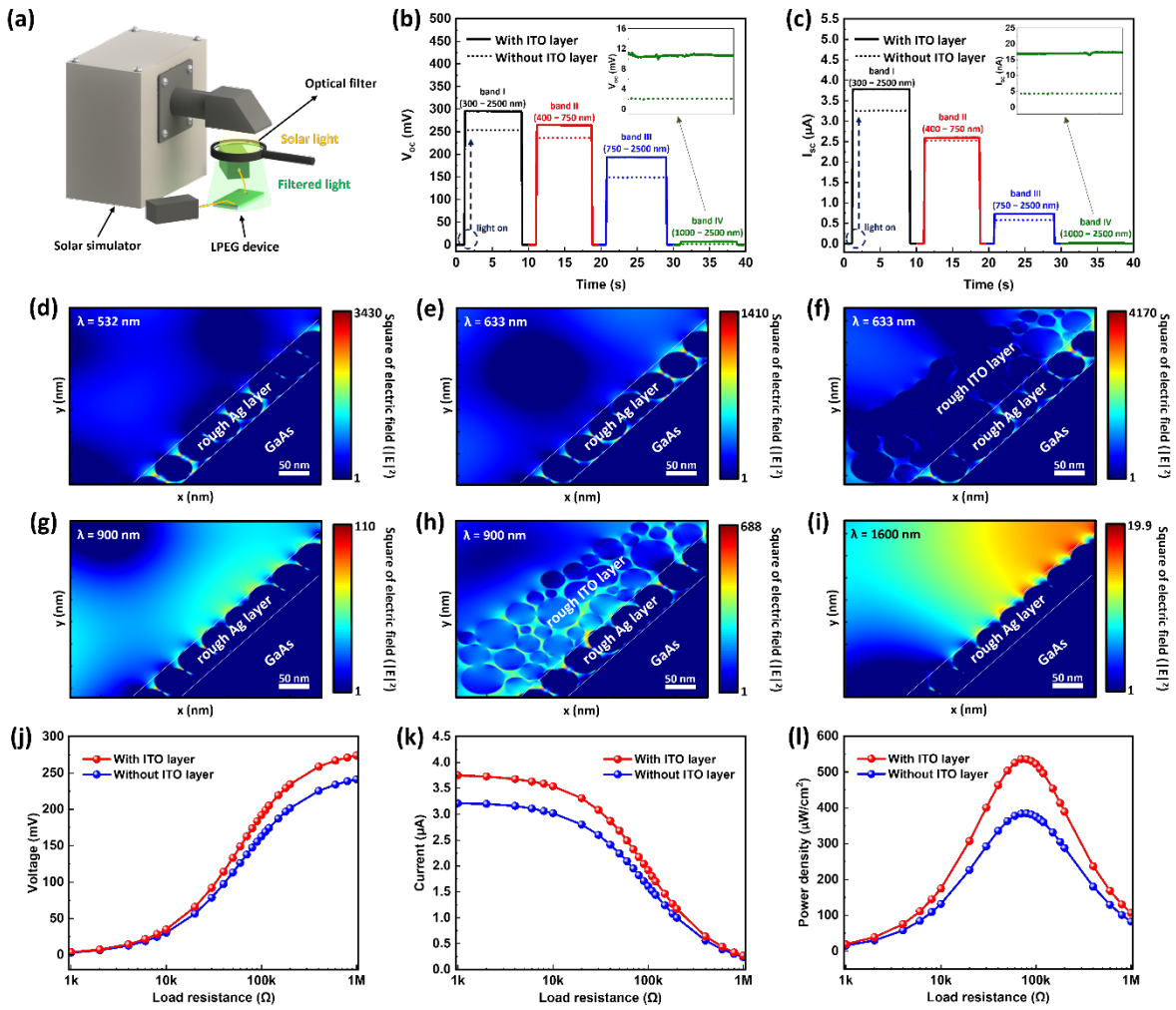

Fig. 3. (a) Schematic diagram of the equipment for measuring the electrical output of the LPEG for different wavelength bands of sunlight using optical filters. The output of (b) open-circuit voltage and (c) short-circuit current of LPEG without and with the ITO layer. FDTD simulation results of the electric field distribution on a logarithmic scale for (d) Ag layer at 532 nm, (e) Ag layer and (f) ITO/Ag layer at 633 nm, (g) Ag layer and (h) ITO/Ag layer at 900 nm, and (i) Ag layer at 1600 nm, respectively. (j) Voltage and (k) current of LPEG without and with ITO layer, with various load resistances ranging from 1 kΩ to 1 MΩ. (l) Power generated by the LPEG with and without the ITO layer calculated by multiplying the voltage and load resistance.

light with a wavelength of 532 nm, the Ag layer generated a stronger electric field than the ITO/Ag layer (Fig. 3(d) and Fig. 1(b)). This is because the SPs are strongly excited by green light when Ag with a roughness size of 60–80 nm is interfaced with air,[48] but when the Ag is interfaced with the ITO, the SPR wavelength is shifted. However, when light of 633 nm wavelength was incident, a stronger electric field was generated in the ITO/Ag layer than in the Ag layer. In general, the SPR wavelength is sensitive to the dielectric properties of the surrounding medium and tends to undergo redshift as the refractive index of the surrounding medium increases.[49,50] Because the ITO has a higher refractive index than air (n_{air}=1),[51,52] the SPR wavelength is redshifted in the Ag layer. For band III, the LPEG with the ITO layer generated V_{oc} of 193 mV and I_{sc} of 730 nA, whereas the LPEG without the ITO layer generated only V_{oc} of 148 mV and I_{sc} of 570 nA. The ITO layer enhanced the voltage and current of the LPEG by 30% and 28%, respectively, compared to the LPEG without the ITO layer. For band IV, the LPEG with the ITO layer generated V_{oc} of 11 mV and I_{sc} of 17 nA, whereas that without the ITO layer generated only V_{oc} of 2 mV and I_{sc} of 4 nA (inset in Fig. 3(b) and (c)). As shown in Fig. 3(b), in Band III, light in the wavelength range of 750–1000 nm contributed the most to the increase in output. This result was probed by simulating the electric field distribution in the Ag layer and ITO/Ag layer at 800 nm and 900 nm, and in the Ag layer at 1600 nm using FDTD, and the results are shown in Fig. S5(a) and (b), and Fig. 3(g)–(i). For incident light at wavelengths of 800 and 900 nm, the ITO/Ag layer (Fig. S5(b) and Fig. 3(h)) enhances the electric field at the interface between the Ag and ITO roughness more than the Ag layer only (Fig. S5(a) and Fig. 3(g)). The SPR wavelength appears to be red-shifted owing to the change in the refractive index of the medium around the Ag layer, and the electric field is enhanced even in the NIR region (800 nm and 900 nm). At the longer wavelength of 900 nm, the electric field hardly increased at the interface between the rough Ag layer and air (Fig. 3(g)), whereas the electric field strengthened between the NPs in the ITO layer (Fig. 3(h)). This explains why the output of the LPEG with the ITO

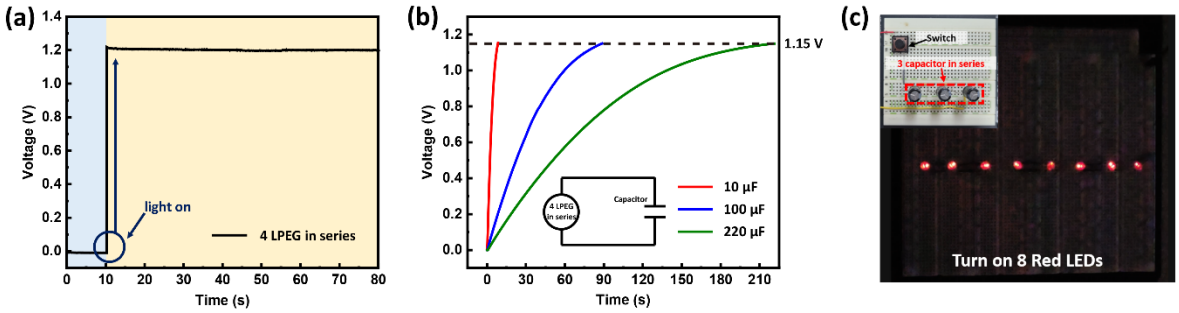

Fig. 4. (a) Output of the open-circuit voltage generated by four LPEGs in series under the solar simulator. (b) Voltage charge curves of the various capacitors by four LPEGs in series. (c) Photographic image of eight red LEDs connected in parallel and powered by the three charged 100 µF capacitors.

layer is higher than that of the LPEG without the ITO layer (Fig. 1(c) and Fig. 3(i)) when light with a wavelength of more than 1000 nm is incident. However, at this longer wavelength, the rate at which the electrical output increases is too low compared to other wavelength bands. This is considered to be a consequence of the incident light in the NIR region exciting the SPs in the ITO layer, but the rate at which the electric field strengthens as a result of the SPs is low compared to that of Ag. Fig. 3(j)–(l) show graphs of the measured voltage, current, and calculated power with external load resistances varying from 1 kΩ to 1 MΩ under a solar simulator to compare the output performance of LPEGs with and without ITO. Regardless of the presence of the ITO layer, as the load resistance increased, the voltage gradually increased and saturated. In contrast, the current gradually decreased with increasing load resistance. The saturated values of the output voltage and current were higher when the ITO layer was present. The power density was calculated using the equation $P = V^2/R$ (where P is the power, V is the output voltage, and R is the load resistance). The maximum power density of the LPEG with the ITO layer is 532.3 µW/cm^2 at a load resistance of 80 kΩ, which is approximately 38% higher than that of the device without the ITO layer (384.6 µW/cm^2 at 80 kΩ).

Fig. 4(a) shows the output voltage generated by four LPEGs, each with an ITO layer, connected in series under the solar simulator. An output voltage of approximately 1.2 V was generated. Hence, a sufficiently high output voltage can be produced by increasing the number of LPEGs connected in series. To store the output energy of the four LPEGs with the ITO layer, 10, 100, and 220 µF capacitors were charged to a constant voltage, and the charging curves are shown in Fig. 4(b). In general, piezoelectric devices require a rectifier because they generate AC output, whereas LPEG generates DC output, so a rectifier is not required in the capacitor-charging circuit (inset in Fig. 4(b)). Four LPEGs connected in series could charge 10 µF, 100 µF, and 220 µF capacitors up to 1.15 V within 8.5 s, 88.6 s, and 221.2 s, respectively, but a degree of voltage loss occurred during the energy storage process. The energy stored in the capacitor was calculated with the equation $E = 1/2 \cdot C \cdot V^2$ (where E is the stored energy, C is the capacitance, and V is the charged voltage), and the input power of the capacitor was calculated by dividing the stored energy by the charging time. For a 100 µF capacitor, the amount of energy stored from four LPEGs in series was approximately 66.125 µJ, and the input power was 0.746 µW. As shown in Fig. 4(c), the energy stored in the capacitors from the LPEGs was used to illuminate red LEDs. Three 100 µF capacitors charged at 1.15 V were connected in series (Fig. 4(c) inset, total 3.45 V) to successfully illuminate eight red LEDs connected in parallel using the stored electrical energy. These results indicate that the piezoelectric energy generated by the SRP can be used to drive small electronic devices.

Conclusions

In summary, we designed a piezoelectric device capable of using a wide range of solar light from the visible to the NIR region using an ITO/Ag double layer. The device was fabricated by sequentially depositing layers to form an ITO/Ag/PZT/Pt/Ti structure on a crater formed on a GaAs (100) wafer using wet chemical etching. Visible and NIR light were shown to excite the SPs in the rough Ag layer and rough ITO layer, respectively, thereby amplifying the electric field on the surface. In response, the amplified SRP deformed the piezoelectric material to generate electrical energy. To analyse the effect of the ITO layer on the electrical output of the LPEG device, optical filters were used to measure the electrical output when visible and NIR light were incident on the device; in both cases, the output voltage and current of the LPEG with the ITO layer were higher than those of the LPEG without the ITO layer. These results were analysed because ITO has both dielectric and metallic properties in the visible and NIR regions, respectively. To explain the experimental results, the electric field distribution in the Ag and ITO layers according to the wavelength of the incident light was confirmed by FDTD simulation, which showed a similar trend to the experimental results. In comparison with the LPEG without the ITO layer, the output power of the LPEG with the ITO layer increased by 38% under the solar simulator. Finally, red LEDs were turned on by storing the electrical energy generated by the serially connected LPEGs in capacitors. These results indicate that piezoelectric devices based on solar radiation could be used to drive various low-power electronic devices.

Author Contributions

J. -H. Ryu: conceptualization, data curation, formal analysis, investigation, methodology, visualization, writing – original draft. H. Y. Lee: data curation, formal analysis, software. S. -H. Kim: investigation, visualization. J. -Y. Lee: formal analysis, visualization. J. -H Jang: data curation, visualization. H. S. Ahn: investigation, funding acquisition, resources. S. -L. Hwang: conceptualization, resources, funding acquisition. R. A. Taylor: conceptualization, data curation, formal analysis, investigation, writing – review & editing. D. H. Ha: data curation, formal analysis, investigation, resources, supervision, validation, writing – review & editing. S. N. Yi: conceptualization, data curation, formal analysis, funding acquisition, project administration, resources, supervision, validation, writing – review & editing.

Conflicts of interest

There are no conflicts to declare.

Acknowledgments

This work was supported by the National Research Foundation of Korea (NRF-2022R1F1A1069919) and Korea Institute for Advancement of Technology (KIAT) grant funded by the Korea Government (MOTIE) (P0012451, The Competency Development Program for Industry Specialist).

References

1 R. Lee, *Science,* 2011, **333**, 569.
2 S. Chu and A. Majumdar, *Nature,* 2012, **488**, 294.
3 K. -W. Lim, M. Peddigari, C. H. Park, H. Y. Lee, Y. Min, J. -W. Kim, C. -W. Ahn, J. -J. Choi, B. -D. Hahn, J. -H. Choi, D. -S. Park, J. -K. Hong, J. -T. Yeom, W.-H. Yoon, J. Ryu, S. N. Yi and G.-T. Hwang, *Energy Environ. Sci.,* 2019, **12**, 666.
4 Z. Sun, X. Chen, Y. He, J. Li, J. Wang, H. Yan and Y. Zhang, *Adv. Energy Mater.,* 2022, **12**, 2200015.
5 D. Zhang, H. Zhang, H. Guo, F. Ye, S. Liu and Y. Wu, *Adv. Funct. Mater.,* 2022, **32**, 2200174.
6 S. Yong, H. Wang, Z. Lin, X. Li, B. Zhu, L. Yang, W. Ding, R. Liao, J. Wang and Z. L. Wang, *Adv. Energy Mater.,* 2022, **12**, 2202469.
7 Z. Deng, L. Xu, H. Qin, X. Li, J. Duan, B. Hou and Z. L. Wang, *Adv. Mater.,* 2022, **34**, 2205064.
8 S. Wu, T. Li, Z. Tong, J. Chao, T. Zhai, J. Xu, T. Yan, M. Wu, Z. Xu, H. Bao, T. Deng and R. Wang, *Adv. Mater.,* 2019, **31**, 1905099.
9 D. Parra, L. Valverde, F. J. Pino and M. K. Patel, *Renew. Sust. Energ. Rev.,* 2019, **101**, 279-294.
10 D. Ginley, M. A. Green and R. Collins, *MRS Bull.,* 2008, **33**, 355.
11 I. E. Khodasevych, L. Wang, A. Mitchell and G. Rosengarten, *Adv. Optical Mater.,* 2015, **3**, 852-881.
12 W. Li, J. Zheng, B. Hu, H.-C. Fu, M. Hu, A. Veyssal, Y. Zhao, J.-H. He, T. L. Liu, A. H. -Baillie and S. Jin, *Nat. Mater.,* 2020, **19**, 1326-1331.
13 V. Kashyap, S. Sakunkaewkasem, P. Jafari, M. Nazari, B. Eslami, S. Nazifi, P. Irajizad, M. D. Marquez, T. R. Lee and H. Ghasemi, *Joule,* 2020, **4**, 1-12.
14 C. Bianchi, L. Niccolai, G. Mengali and A. A. Quarta, *Aerosp. Sci. Technol.,* 2021, **119**, 107150.
15 J. Homola, S. S. Yee and G. Gauglitz, *Sens. Actuators B Chem.,* 1999, **54**, 3-15.
16 Z. Zhang, Y. Fang, W. Wang, L. Chen and M. Sun, *Adv. Sci.,* 2016, **3**, 1500215.
17 S. -H. Kim, H. Y. Lee, J. -H. Ryu, J. -Y. Lee, H. -S. Kim, H. S. Ahn, D. H. Ha and S. N. Yi, *J. Mater. Sci.,* 2022, **57**, 7547-7555.
18 P. Pandey, S. Vongphachanh, J. W. Yoon, B. Y. Kim, C. -J. Choi, J. I. Sohn and W. -K. Hong, *J. Alloys Compd.,* 2021, **859**, 157862.
19 K. L. Kelly, E. Coronado, L. L. Zhao and G. C. Schatz, *J. Phys. Chem. B,* 2003, **107**, 668-677.
20 F. Tam, C. Moran and N. Halas, *J. Phys. Chem. B,* 2004, **108**, 17290-17294.
21 K. Liu, Y. Bai, L. Zhang, Z. Yang, Q. Fan, H. Zheng, Y. Yin and C. Gao, *Nano Lett.,* 2016, **16**, 3675-3681.
22 D. Banerjee, X. Guo and S. G. Cloutier, *Sol. RRL,* 2018, **2**, 1800007.
23 J. Lee, B. Hua, S. Park, M. Ha, Y. Lee, Z. Fan and H. Ko, *Nanoscale* 2014, **6**, 616.
24 H. Hao, L. Wang, X. Ma, K. Cao, H. Yu, M. Wang, W. Gu, R. Zhu, M. S. Anwar, S. Chen and W. Huang, *Sol. RRL,* 2018, **2**, 1800061.
25 M. A. Noginov, L. Gu, J. Livenere, G. Zhu, A. K. Pradhan, R. Mundle, M. Bahoura, Y. A. Barnakov and V. A. Podolskiy, *Appl. Phys. Lett.,* 2011, **99**, 021101.
26 G. V. Naik, J. Kim and A. Boltasseva, *Opt. Mater. Express,* 2011, **1**, 1090-1099.
27 J. H. Kim, B. D. Ahn, C. H. Lee, K. A. Jeon, H. S. Kang, G. H. Kim and S. Y. Lee, *Thin Solid Films,* 2007, **515**, 3580-3583.
28 G. V. Naik, V. M. Shalaev and A. Boltasseva, *Adv. Mater.,* 2013, **25**, 3264-3294.
29 X. Fang, C. L. Mak, J. Dai, K. Li, H. Ye and C. W. Leung, *ACS Appl. Mater. Interfaces,* 2014, **6**, 15743-15752.
30 P. R. West, S. Ishii, G. V. Naik, N. K. Emani, V. M. Shalaev and A. Boltasseva, *Laser Photonics Rev.,* 2010, **4**, 795-808.
31 K. K. Lam, S. M. Ng, H. F. Wong, L. Fei, Y. Liu, K. H. Chan, H. Ye, C. W. Leung and C. L. Mak, *ACS Appl. Mater. Interfaces,* 2020, **12**, 13437-13446.
32 P. Guo, R. D. Schaller, L. E. Ocola, B. T. Diroll, J. B. Ketterson and R. P. H. Chang, *Nat. Commun.,* 2016, **7**, 12892.
33 C. Chen, Z. Wang, K. Wu, H. Chong, Z. Xu and H. Ye, *ACS Appl. Mater. Interfaces,* 2018, **10**, 14886-14893.
34 R. Hong, X. Wang, J. Ji, C. Tao, D. Zhang and D. Zhang, *Appl. Surf. Sci.,* 2015, **356**, 701-706.
35 K. Ma, N. Zhou, M. Yuan, D. Li and D. Yang, *Nanoscale Res. Lett.,* 2014, **9**, 547.
36 R. Hong, W. Shao, W. Sun, C. Deng, C. Tao and D. Zhang, *Opt. Mater.,* 2018, **83**, 212-219.
37 H. Y. Lee, M. S. Kwak, K. -W. Lim, H. S. Ahn, G. -T. Hwang, D. H. Ha, R. A. Taylor and S. N. Yi, *Opt. Express*, 2021, **29**, 35161.
38 H. Y. Lee, M. S. Kwak, G. -T. Hwang, H. S. Ahn, D. H. Ha and S. N. Yi, *Appl. Surf. Sci.,* 2022, **596**, 153588.
39 H. Y. Lee, M. S. Kwak, G.-T. Hwang, H. S. Ahn, R. A. Taylor, D. H. Ha, and S. N. Yi, *Adv. Optical Mater.*, submitted.
40 J. Cui, Y. Li, L. Liu, L. Chen, J. Xu, J. Ma, G. Fang, E. Zhu, H. Wu, L. Zhao, L. Wang and Y. Huang, *Nano Lett.,* 2015, **15**, 6295-6301.
41 J. Kim, S. Baek, J. Y. Park, K. H. Kim and J. -L. Lee, *Small* 2021, **17**, 2100654.
42 H. Y. Lee, M. S. Kwak, K. -W. Lim, H. S. Ahn and S. N. Yi, *Korean J. Mater. Res.* 2019, **29**, 155-159.
43 X. Y. Zhang, X. Zhao, C. W. Lai, J. Wang, X. G. Tang, and J. Y. Dai, *Appl. Phys. Lett.,* 2004, **85**, 4190.
44 E. R. Camargo, J. Frantti and M. Kakihana, *J. Mater. Chem.,* 2001, **11**, 1875-1879.
45 K.-I. Park, C. K. Jeong, J. Ryu, G.-T. Hwang and K. J. Lee, *Adv. Energy Mater.,* 2003, **3**, 1539-1544.
46 H. Wei and H. Xu, *Nanoscale,* 2013, **5**, 10794.
47 H. Liang, Z. Li, W. Wang, Y. Wu and H. Xu, *Adv. Mater.,* 2009, **21**, 4614–4618.
48 D. D. Evanoff Jr., G and Chumanov, *ChemPhysChem,* 2005, **6**, 1221–1231.

49 M. M. Miller and A. A. Lazarides, *J. Phys. Chem. B,* 2005, **109**, 21556-21565.
50 F. Tam, C. Moran and N. Halas, *J. Phys. Chem. B,* 2004, **108**, 17290-17294.
51 Y. Yang, X.W. Sun, B.J. Chen, C.X. Xu, T.P. Chen, C.Q. Sun, B.K. Tay and Z. Sun, *Thin Solid Films,* 2006, **510**, 95-101.
52 M. Baum, I. Alexeev, M. Latzel, S. H. Christiansen and M. Schmidt, *Opt. Express*, 2013, **21**, 22754.

